



Fast neutron background characterization of the future RICOCHET experiment at the ILL research nuclear reactor

C. Augier¹, G. Baulieu¹, V. Belov⁸, L. Berge², J. Billard^{1,a}, G. Bres⁷, J.-L. Bret⁷, A. Broniatowski², M. Calvo⁷, A. Cazes¹, D. Chaize¹, M. Chapellier², L. Chaplinsky⁶, G. Chemin³, R. Chen⁴, J. Colas¹, M. De Jesus¹, P. de Marcillac², L. Dumoulin², O. Exshaw⁷, S. Ferriol¹, E. Figueroa-Feliciano⁴, J.-B. Filippini¹, J. A. Formaggio⁵, S. Fuard¹¹, J. Gascon¹, A. Giuliani², J. Goupy⁷, C. Goy³, C. Guerin¹, E. Guy¹, P. Harrington⁵, S. T. Heine⁵, S. A. Hertel⁶, M. Heusch³, C. F. Hirjibehedin⁹, Z. Hong¹⁰, J.-C. Ianigro¹, Y. Jin¹², J. P. Johnston⁵, A. Juillard¹, D. Karaivanov⁸, S. Kazarcev⁸, J. Lamblin³, H. Lattaud¹, M. Li⁵, A. Lubashevskiy⁸, S. Marnieros², D. W. Mayer⁵, J. Minet⁷, D. Misiak¹, J.-L. Mocellin⁷, A. Monfardini⁷, F. Mounier¹, W. D. Oliver⁹, E. Olivieri², C. Oriol², P. K. Patel⁶, E. Perbet³, H. D. Pinckney⁶, D. Poda², D. Ponomarev⁸, F. Rarbi³, J.-S. Real³, T. Redon², A. Robert¹¹, S. Rozov⁸, I. Rozova⁸, T. Salagnac¹, V. Sanglard¹, B. Schmidt⁴, Ye. Shevchik⁸, V. Sibille^{1,5,b}, T. Soldner¹¹, J. Stachurska⁵, A. Stutz³, L. Vagneron¹, W. Van De Pontseele⁵, F. Vezzu³, S. Weber⁹, L. Winslow⁵, E. Yakushev⁸, D. Zinatulina⁸, the Ricochet Collaboration

¹ Univ Lyon, Université Lyon, 1, CNRS/IN2P3, IP2I-Lyon, 69622 Villeurbanne, France

² Université Paris-Saclay, CNRS/IN2P3, IJCLab, 91405 Orsay, France

³ Univ. Grenoble Alpes, CNRS, Grenoble INP, LPSC-IN2P3, 38000 Grenoble, France

⁴ Department of Physics and Astronomy, Northwestern University, Evanston, IL, USA

⁵ Laboratory for Nuclear Science, Massachusetts Institute of Technology, Cambridge, MA 02139, USA

⁶ Department of Physics, University of Massachusetts at Amherst, Amherst, MA 02139, USA

⁷ Univ. Grenoble Alpes, CNRS, Grenoble INP, Institut Néel 38000, 38000 Grenoble, France

⁸ Department of Nuclear Spectroscopy and Radiochemistry, Laboratory of Nuclear Problems, JINR, Dubna, Moscow Region 141980, Russia

⁹ Lincoln Laboratory, Lexington, MA, USA

¹⁰ Department of Physics, University of Toronto, Toronto, ON M5S 1A7, Canada

¹¹ Institut Laue Langevin, 38042 Grenoble, France

¹² C2N, CNRS, Univ. Paris-Saclay, 91120 Palaiseau, France

Received: 2 August 2022 / Accepted: 21 December 2022 / Published online: 14 January 2023
© The Author(s) 2023

Abstract The future RICOCHET experiment aims at searching for new physics in the electroweak sector by providing a high precision measurement of the Coherent Elastic Neutrino-Nucleus Scattering (CENNS) process down to the sub-100 eV nuclear recoil energy range. The experiment will deploy a kg-scale low-energy-threshold detector array combining Ge and Zn target crystals 8.8 m away from the 58 MW research nuclear reactor core of the Institut Laue Langevin (ILL) in Grenoble, France. Currently, the RICOCHET Collaboration is characterizing the backgrounds at its future experimental site in order to optimize the experiment's shielding design. The most threatening background component, which cannot be actively rejected by particle identification, consists of keV-scale neutron-induced nuclear recoils. These initial fast neutrons are generated by the reactor core and surround-

ing experiments (reactogenics), and by the cosmic rays producing primary neutrons and muon-induced neutrons in the surrounding materials. In this paper, we present the RICOCHET neutron background characterization using ³He proportional counters which exhibit a high sensitivity to thermal, epithermal and fast neutrons. We compare these measurements to the RICOCHET Geant4 simulations to validate our reactogenic and cosmogenic neutron background estimations. Eventually, we present our estimated neutron background for the future RICOCHET experiment and the resulting CENNS detection significance. Our results show that depending on the effectiveness of the muon veto, we expect a total nuclear recoil background rate between 44 ± 3 and 9 ± 2 events/day/kg in the CENNS region of interest, i.e. between 50 eV and 1 keV. We therefore found that the RICOCHET experiment should reach a statistical significance of 4.6 to 13.6σ for the detection of CENNS after one reactor

^a e-mail: j.billard@ipnl.in2p3.fr (corresponding author)

^b e-mail: vsibille@mit.edu

cycle, when only the limiting neutron background is considered.

1 Introduction

Coherent elastic neutrino-nucleus scattering (CENNS) was predicted in 1974 [1] and observed experimentally for the first time in 2017 [2]. This elastic scattering process, inducing nuclear recoils of a few keV at most, proceeds via the neutral weak current and benefits from a coherent enhancement proportional to the square of the number of neutrons [1], suggesting that even a kg-scale experiment, located in the proximity of a research or commercial nuclear reactor, can observe a sizable neutrino signal. The search for physics beyond the Standard Model with CENNS requires to measure with the highest level of precision the sub-100 eV energy range of the induced nuclear recoils, as most new physics signatures induce energy spectral distortions in this energy region [3]. These include for instance the existence of sterile neutrinos and of new mediators that could be related to the long lasting Dark Matter problem, and the possibility of Non Standard Interactions that would dramatically affect our understanding of the electroweak sector.

Thanks to its exceptionally rich science program, CENNS has led to significant worldwide experimental efforts over the last decades, with several ongoing and planned dedicated experiments based on a host of techniques. Most of these experiments are, or will be, located at nuclear reactor sites producing low-energy neutrinos with mean energies of about 3 MeV: CONNIE using Si-based CCDs [4]; TEXONO [5], NuGEN [6], CONUS [7], and NCC-1701 [8] using ionization-based Ge semiconductors; and MINER [9], NuCLEUS [10], and RICOCHET [11] using cryogenic detectors. Only the COHERENT experiment [2, 12] is looking at higher neutrino energies of about 30 MeV in average produced by the Spallation Neutron Source (SNS) in Oak Ridge, and experiments are planned at the European Spallation Source (ESS) in Lund [13].

The RICOCHET experiment seeks to utilize a kg-scale cryogenic detector payload combining Zn and Ge target crystals with sub-100 eV energy threshold and particle identification capabilities down to the energy threshold to reject the dominating gamma-induced electronic recoil background. Such identification will be achieved thanks to the double heat-and-ionization measurement with the semiconducting Ge target, and pulse shape discrimination in the superconducting Zn crystals. In this context, the neutron-induced nuclear recoils are therefore expected to be the limiting background to the future RICOCHET experiment which will be located near the nuclear reactor of the Institut Laue Langevin (ILL). The close proximity to the reactor core comes at the cost of an additional reactor-correlated fast neutron background, called

reactogenic neutrons, which could mimic a CENNS signal in the Ge and Zn target detectors hence limiting the expected RICOCHET CENNS sensitivity at ILL.

In this paper we present our fast neutron background characterization of the ILL-H7 site, where RICOCHET will be installed, and its implication on the expected background levels of the future RICOCHET experiment. To do so, we compare data taken with a ^3He proportional counter sensitive to both thermal and fast neutrons with Geant4 simulations. Additionally, as a proof of concept of the presented method we also characterized the cosmogenic neutron background at the *Institut de Physique des 2 Infinis de Lyon* (IP2I) cryogenic test facility, where Ge bolometers with particle identification capabilities have been operated [14, 15]. We show that this low-radioactivity ^3He proportional counter is well-suited to constrain the fast neutron background at the future RICOCHET experiment. In light of these results, we conclude with the RICOCHET shielding optimization and the anticipated nuclear recoil background induced by reactogenic and cosmogenic neutrons.

2 The Ricochet experiment

The future RICOCHET experiment will be deployed at the ILL-H7 site (see Fig. 1). The H7 site starts at about 7 m from the ILL reactor core that provides a nominal thermal power of 58.3 MW, leading to a neutrino flux at the RICOCHET detectors, 8.8 m from the reactor core, of about $1.1 \times 10^{12} \text{ cm}^{-2} \text{ s}^{-1}$ which corresponds to a CENNS event rate of approximately 12.8 and 11.2 events/kg/day with a 50 eV energy threshold and Ge and Zn targets crystal, respectively. The reactor is operated in cycles of typically 50 days duration with reactor-off periods sufficiently long to measure reactor-independent backgrounds with high statistics, including internal radioactivity and cosmogenic-induced backgrounds. The ILL-H7 experimental site is about 3 m wide, 6 m long and 3.5 m high. It is located below a water channel providing about 15 m.w.e. against cosmic radiation. It is not fed by a neutron beam and is well-shielded against irradiation from the reactor and neighboring instruments (IN20 and D19). The site has been used successfully for the neutrino experiment STEREO from 2016 to 2020 [16, 17].

The RICOCHET shielding will be divided into two parts: a 300 K outer shielding and a cryogenic inner one. The outer shielding will be composed of a 35 cm thick layer of 3%-borated polyethylene to thermalize and capture fast neutrons surrounded by a 20 cm thick layer of lead to mitigate the gamma flux. Additionally, another 35 cm thick layer of polyethylene will be positioned on top of it to further reduce the cosmogenic fast neutron flux. The whole setup will be surrounded with 0.5 cm thick soft iron to reduce the magnetic stray field originating from neighboring experiments. This

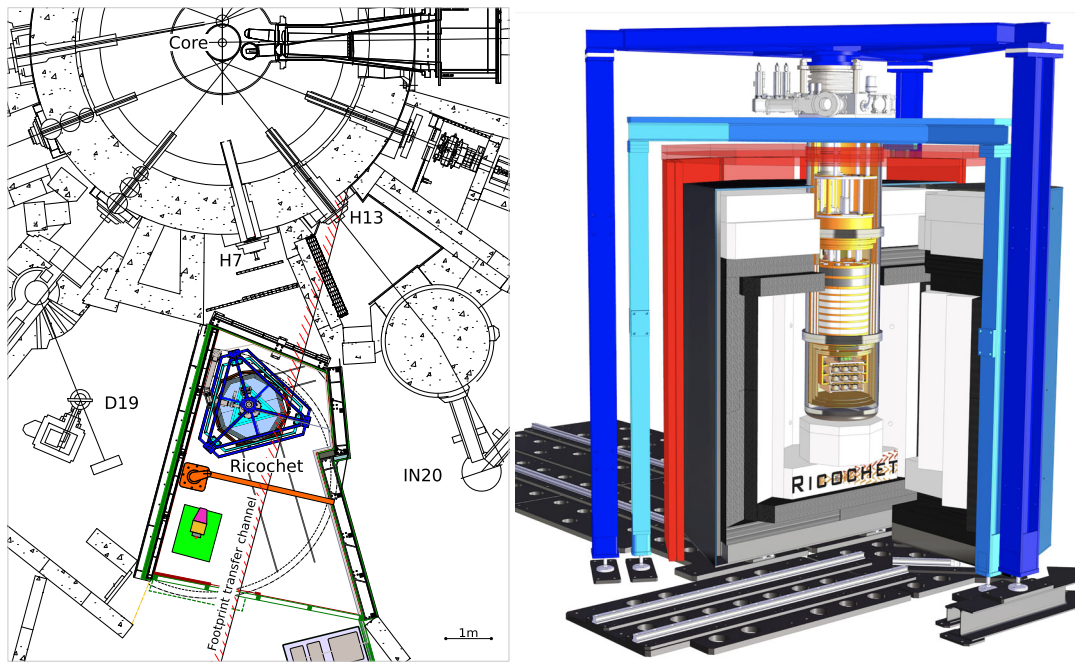


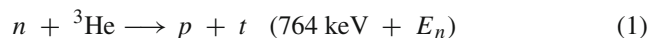
Fig. 1 Left: schematic of the planned RICOCHET integration within the ILL-H7 experimental site. The cryostat is mechanically anchored thanks to two triangle-shaped frames surrounding the passive shielding and active muon veto. Also shown are the 1-t crane (orange), the pulsed DT-based low-energy and mono-energetic neutron source in its storage position (light green), and the surrounding IN20 and D19 experiments.

Right: drawing of the future RICOCHET experiment. The Hexa-Dry 200 Ultra-quiet cryostat from CryoConcept is held by two mechanically decoupled frames (dark and light blue) and is surrounded by its outer external shielding layers of polyethylene (white), lead (gray) and soft iron (black). The muon veto is shown as the red panels on the top and side of the setup

outer shielding will be divided into three sections installed on rails to allow for an easy access to the cryostat. Lastly, muon-induced gamma and neutron backgrounds will be further reduced thanks to a surrounding muon veto, made of two layers of 3 cm thick plastic scintillator, to reject events in temporal coincidence with detected muons. The cryogenic inner shielding, installed inside the cryostat above the detectors and composed of a 8.5 cm thick layer of lead and a 21 cm thick layer of polyethylene, with interleaved 1 cm thick copper layers, will ensure a closed shielding. Additionally, 8 mm thick polyethylene layers mounted on each thermal screen will further improve the shielding tightness. Eventually, up to two 1 mm thick layers of mumetal will also be added between thermal screens to further reduce the residual magnetic field from adjacent experiments for optimal operation of the Zn cryogenic detectors that use superconducting quantum interference devices (SQUIDS) [11]. Note that the muon veto will also include a cryogenic portion at 50 K to avoid a significant gap in veto coverage at the crossing of the cryostat. According to our cosmogenic simulations, such a muon veto should exhibit a muon-induced trigger rate of about 400 Hz which will be manageable with our $\sim 100 \mu\text{s}$ timing resolution bolometers, requiring coincidence time windows of $O(1)$ ms, with a reasonable livetime loss of less than 30% [15].

3 Thermal and fast neutron detection with a low-radioactivity ^3He proportional counter

To characterize the neutron background at the ILL-H7 site, we used a proportional counter tube filled with ^3He gas. The thermal and fast neutrons are detected via the following on-flight capture reaction:



where E_n is the neutron kinetic energy. The $^3\text{He}(n,p)$ cross section for thermal neutrons is $\sigma = 5333 \pm 7 \text{ b}$ [18] and drops below several barns for neutron energies between 100 keV and 10 MeV where elastic scattering becomes relevant [19]. The CHM-57 counter [20] used in this work has an active length of 860 mm with an internal diameter of 31 mm. The counter is filled with 400 kPa of ^3He and 500 kPa of ^{40}Ar , where the latter gas element is used as a quencher in order to stabilize the avalanche process of the proportional chamber following an ionization signal detection. Intrinsic backgrounds from alpha decays of U and Th progenies in the walls were reduced by covering the detector's inner walls with 50–60 μm of Teflon and 1 μm of electrolytic copper [20]. The

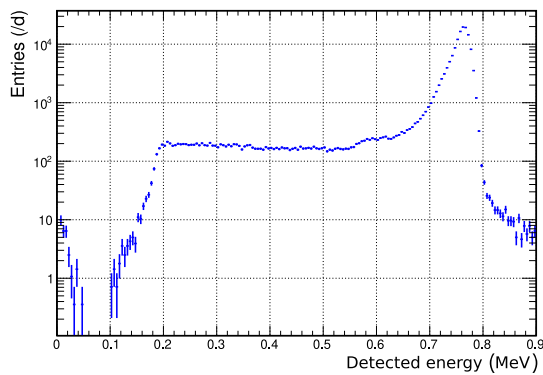
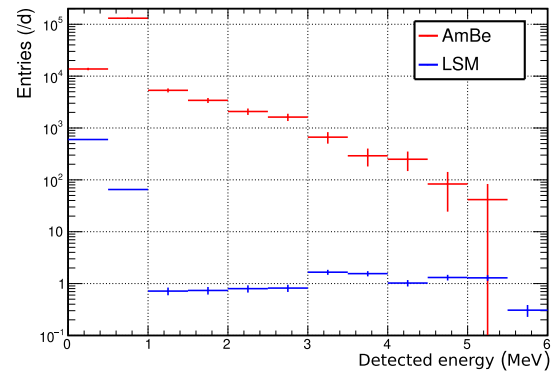


Fig. 2 Left: measured energy spectrum below 900 keV, covering the so-called thermal neutron capture energy region, taken at the ILL-H7 site without thermal neutron shielding surrounding the ^3He counter and while the nuclear reactor was in operation. Right: measured energy spectra up to 6 MeV obtained after 49 days of data taking at the Modane underground laboratory (blue) and during a few hours of neutron calibration, using an AmBe source emitting 2×10^6 neutron per second



positioned at 1 m from the detector, done at the IP2I (red). Note that events appearing above 1 MeV are expected to be produced by fast neutrons from both elastic scattering, predominantly on ^3He , and on-flight captures also on ^3He . In the case of the AmBe neutron calibration a 5 mm thick B₄C loaded rubber was surrounding the detector in order to avoid spectral distortions arising from thermal capture pile-up events

ionization signal, predominantly driven by the drifting ions to the external cathode, is read out by an attached Cremat CR-110 single channel charge-sensitive preamplifier. The preamplified signal is then analyzed online by a DT5780 digitizer working in pulse height analysis mode.¹

A typical thermal neutron calibration spectrum is shown in Fig. 2 (left panel). The expected 764 keV peak from thermal neutron captures is clearly visible. A broad plateau at lower energies is also seen, resulting from captures occurring near the wall of the counter, where either the triton (t) or proton (p) escapes without depositing its full energy. From Fig. 2 (left panel) two shoulder-like structures, due to this so-called wall effect, are clearly visible at 191 keV and 573 keV which respectively correspond to the full collection of only the triton or proton recoils. These three characteristic features in the energy spectrum, at 191 keV, 573 keV and 764 keV, have been used to cross-check the energy scale and linearity of the detector response [20]. According to SRIM-based simulations [21], and further confirmed with our Geant4 simulations detailed in Sect. 4.1, the averaged proton and triton track lengths following a thermal neutron capture on ^3He are about 2 mm and 0.7 mm, respectively.

In this work, we focus on the high energy portion of the observed energy spectrum, i.e. above 1 MeV in detected energy, in order to estimate the fast component of the neutron background at the ILL reactor. For energies beyond 1 MeV, we expect events to be predominantly due to elastic and inelastic (on-flight captures) scatterings of fast neutrons on ^3He . Note that elastic scatterings on ^{40}Ar nuclei are expected to have a negligible contribution to the observed energy spectrum beyond 1 MeV as these would require neutron ener-

gies above 20 MeV due to both kinematics and their 50%-60% ionization yield at a few MeV in recoiling energy (see Sect. 4.1). Also, thanks to their much lower stopping power, gamma induced electronic recoils cannot deposit more than a few hundreds of keV in the detector volume. Eventually, the only relevant background beyond 1 MeV of detected energy is coming from alpha decays with degraded energies arising from residual radioactive contaminants. As mentioned above, this ^3He proportional counter has been designed to minimize such contamination in order to offer a maximal sensitivity to fast neutron detection.

Figure 2 (right panel) shows two observed energy spectra obtained with this counter when it was irradiated by a fast neutron source of AmBe (red) and when it was operated in the low-background Modane underground laboratory (LSM) [22] (blue). Focusing on the energy range above 1 MeV, where we expect to detect fast neutrons, we see a clear excess of events during the AmBe calibration with respect to the low-background measurement performed at LSM. Based on previous neutron measurements done at LSM [23], the observed events beyond 1 MeV are understood as residual radon contamination, resulting in a flat background of 2 events/day/MeV that will ultimately limit our neutron detection sensitivity, see Sect. 5.1.

In order to validate our approach of using the observed energy spectrum above 1 MeV to estimate the fast neutron background, we performed two additional cross checks of the detector response dedicated to the linearity of the energy scale and its sensitivity to the incoming neutron direction. As the deposited energy increases, one can expect to observe so-called space charge effects corresponding to a degradation of the amplification gain due to charge screening [24]. The latter is directly related to the amplification gain, such that

¹ For more details see <https://www.caen.it/products/dt5780/>.

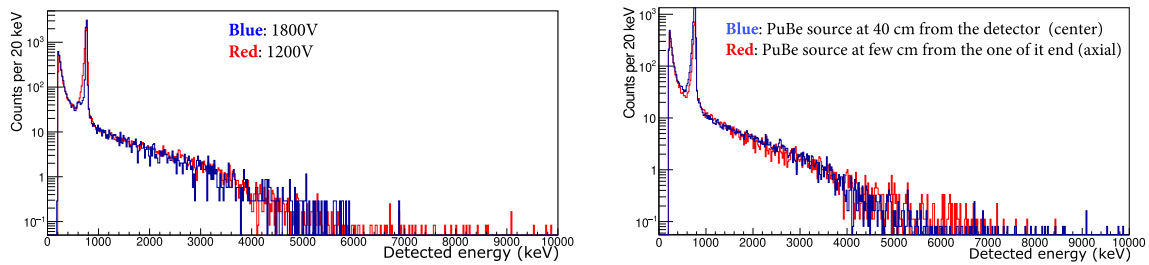


Fig. 3 Left: observed energy spectra with the ^3He counter irradiated by a PuBe neutron calibration source with two different amplification voltages of 1200 V (red) and 1800 V (blue) for which the avalanche

amplification gains differ by a factor of about 6. Right: same as left panel but with a fixed voltage of 1200 V and the neutron source either irradiating the counter along its axial (red) or radial axis (blue)

a larger gain would lead to higher charge screening due to a larger number of electrons produced in the avalanche process. Figure 3 (left panel) shows two measurements where the voltage was varied from 1200 to 1800 V, corresponding to an amplification gain variation of about 6. Because we observe no statistically significant change in the spectrum under this widely varied gain, the 1650 V operating voltage is taken to be in the linear regime, at least for our region of interest up to 10 MeV. Note that variations of the ionization yield as a function of the recoil energy of ^3He , proton, and triton could also lead to non-linearity in the energy-scale. However, SRIM simulations of all three nuclei from 500 keV up to 10 MeV of recoiling energy, in 400 kPa of ^3He and 500 kPa of ^{40}Ar gas, predict an ionization yield between 98.3% and 100% with negligible energy dependence (see Sect. 4.1). Additionally, these simulated ionization yield results are further supported by the experimental observation from [19] where a similar ^3He -based proportional counter and monoenergetic neutrons with energies up to 17.5 MeV were used and no significant variations in the ionization yields of p, t, and ^3He was found.

The fast neutron flux is expected to be anisotropic at the ILL-H7 reactor site and several localised sources have been identified in previous measurements done by the STEREO Collaboration [16]. Therefore, we investigated the response of our detector to a neutron calibration source irradiating our detector in two extreme orientations: centered along its z axis with a radial orientation, and positioned at the bottom end-cap of the detector offering an axial orientation. The resulting energy spectra are shown in Fig. 3 (right panel) for the radial (blue) and axial (red) neutron source irradiation orientations. From the comparison of these two extreme cases, we only observe a marginal difference at the highest energies, i.e. above 6 MeV. This is explained by the improved full collection efficiency of the recoiling nuclei when their tracks are aligned with the detector axis.

Based on these results, we can conclude that our ^3He proportional counter is well-suited to measure and characterize

the fast neutron component of the ILL-H7 reactor site where the future RICOCHET experiment will be deployed.

4 Geant4 simulations

The goal of this work is to compare our observed energy spectra to simulated ones in various conditions and from different sites, both in terms of shape and rate. Therefore, in the following section we discuss the details of our simulations. Those include both the simulation of the ^3He counter response and of the different cosmic and reactor neutron sources. All of the following simulations have been done within the Geant4 10.06.p02 software considering the “Shielding” physics list [25].

4.1 ^3He proportional counter simulation

The ^3He proportional counter is simulated according to its geometry and gas composition as described previously. Based on our observed ~ 30 keV energy resolution (RMS) at the 764 keV line, far smaller than the considered bin width of 250 keV when compared to our measured spectra, and the negligible space charge effect, we did not include these finite detector response effects in our simulations. However, note that the physics list incorporates the “G4ScreenedNuclearRecoil” module that models screened electromagnetic nuclear elastic scattering, as required for an accurate simulation of the propagation of the proton and triton after a neutron capture on ^3He or following any elastic scattering happening in the proportional counter [26]. Lastly, using SRIM-based recoil simulations of proton, triton, ^3He and Ar from 500 keV up to 10 MeV, we found the ionization yield of the three lighter nuclides to be greater than 98.3% (at 500 keV) and rising up to almost 100% at 10 MeV. For the Ar recoils however, we found the ionization yield to be of 48.5% at 500 keV and constantly rising up to 93.5% at 10 MeV [21]. Taking into account recoil kinematics and a

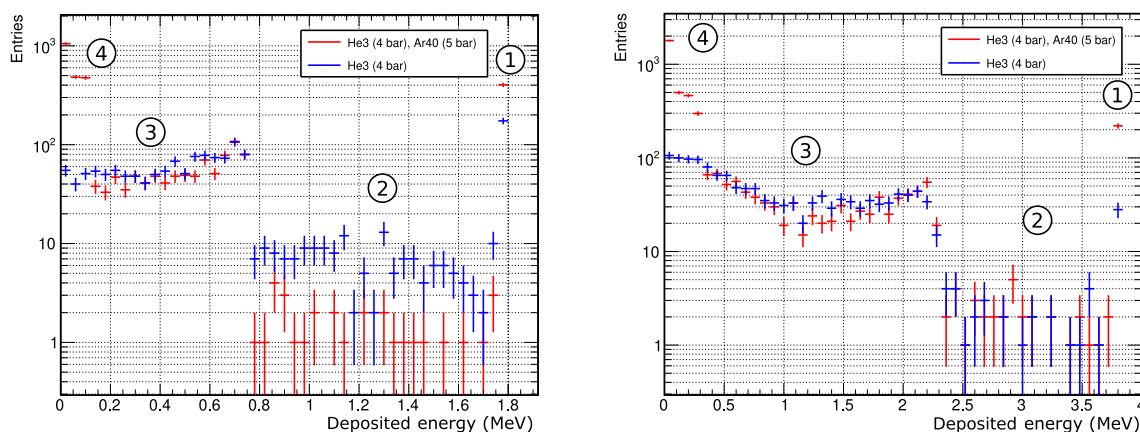


Fig. 4 Simulations of the ^3He proportional counter response to an isotropic mono-energetic neutron flux of 1 MeV (left) and 3 MeV (right). The resulting spectra are shown in two configurations: a pure ^3He gas

at 400 kPa (blue) and the gas mixture corresponding to our detector gas composition made of 400 kPa of ^3He + 500 kPa of ^{40}Ar (red)

1 MeV energy threshold in detected energy, we expect to only be sensitive to p, t, and ^3He recoils for which we can assume that the ionization yield is constant and that the detected energy is equivalent to the kinetic recoil energy.

Geant4 simulations were performed in which monoenergetic neutron fluxes were isotropically incident on the ^3He proportional counter. Figure 4 presents the resulting energy spectra for incident neutron energies of 1 MeV (left panel) and 3 MeV (right panel). Both panels present the results with two gas compositions: pure ^3He gas at 400 kPa (blue) and the actual gas mixture of our detector made of 400 kPa of ^3He and 500 kPa of ^{40}Ar (red). For both panels we see four characteristic features: 1) a line at $E_n + 764$ keV corresponding to on-flight neutron captures fully collected in the detector volume, 2) on-flight neutron captures happening near the wall of the detector with lowered energies deposited inside the gas, 3) a rather flat ^3He recoil energy spectrum with its corresponding endpoint at $\frac{3}{4}E_n$, and 4) a low-energy ^{40}Ar recoil energy spectrum contribution with its expected endpoint at $0.1 \times E_n$ (when ^{40}Ar gas is added to the mixture). Interestingly we see that the addition of the 500 kPa of ^{40}Ar gas has very little effect on the observed energy spectrum of the ^3He recoils but has the benefit of increasing the peak-to-continuum ratio of on-flight neutron captures, hence improving the spectroscopic ability of the detector. This is explained by the fact that this additional gas component increases the fraction of fully collected proton + triton tracks by increasing the pressure hence reducing the recoiling nuclei track lengths. As a conclusion of these simulations, we expect our proportional counter to exhibit some neutron spectroscopic capabilities (i.e. direct neutron energy measurement) even though these are attenuated by the ^3He recoil contributions from neutron elastic scatterings and by incomplete track collections. In spite of these limitations, Fig. 4 illustrates the capability of

our detector to assess the fast neutron flux at the RICOCHET experiment, both in energy dependence and magnitude (see Sect. 5).

4.2 Cosmogenic and reactogenic neutrons

The RICOCHET experiment will be using low-radioactivity materials such that the internal radioactivity is expected to be sub-dominant with respect to the external cosmogenic and reactogenic neutrons. To simulate the cosmogenic neutrons at the various sites of interest, we used the Cosmic-ray shower library (CRY) that generates correlated cosmic-ray particle shower distributions for use as input to our Geant4 transport and detector simulation codes [27]. We considered the latitudes of Grenoble for the ILL-based simulations and of Lyon for the IP21-based simulations that are relevant for the geomagnetic cut-off. Additionally, the live-time simulated by CRY with its otherwise default settings has been divided by 1.28 for the ILL site, as suggested by past muon flux measurements at the ILL-H7 site [16].

Concerning the reactogenic neutrons at ILL, we used simulations performed by the STEREO Collaboration. From the background measurements done in preparation to the STEREO experiment [16], the main source of reactogenic background identified was the IN20 experiment and, more specifically, the corresponding neutron beam H13 and its shutters. Using a MCNP code [29], the reactor neutron energy spectrum has been propagated through the H13 tube and the IN20 experimental site to estimate the energy spectrum and rates at the STEREO location [28]. However, the geometry did not include some shielding walls that were added since. Therefore, we expect the energy spectrum to be overestimated and we consider it as a conservative upper limit.

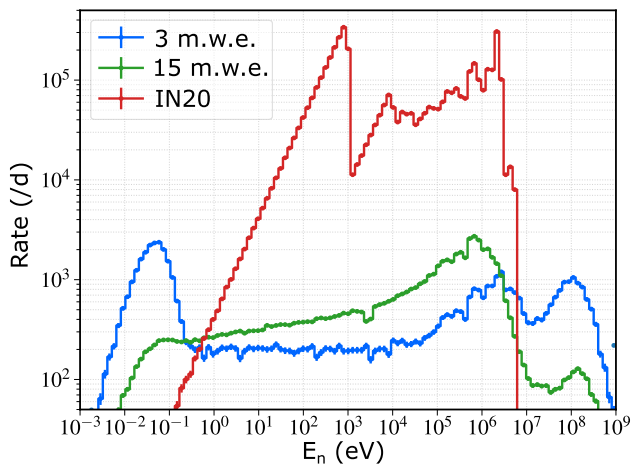


Fig. 5 Simulated neutron fluxes entering the ^3He detector per day as a function of energy for the reactogenic (IN20 – red from [28]), and the cosmogenic neutrons component at the two different locations considered in this work: IP2I surface lab with a ~ 3 m.w.e. of overburden (blue), and the ILL-H7 reactor site with its mean 15 m.w.e. of overburden (green). Note that the binning along the x-axis is logarithmic

The overall normalization of the flux is 790 neutrons/ m^2/s at reactor nominal power.

Figure 5 shows the simulated reactogenic and cosmogenic neutron spectra entering the ^3He proportional counter. The reactogenic spectrum was obtained at 58 MW nominal thermal power for a box-like generation surface of 56 m^2 (IN20 – red). The cosmogenic spectra are from two different locations: IP2I surface lab with its averaged overburden of ~ 3 m.w.e. (see Sect. 7 – blue), and the ILL-H7 reactor site with its mean 15 m.w.e. of overburden (green) [16]. In the IP2I surface lab case we can clearly identify the four usual cosmic neutron populations: thermal ($E_n < 0.5$ eV), epithermal (0.5 eV $< E_n < 0.1$ MeV), evaporation (0.1 MeV $< E_n < 20$ MeV), and cascade ($E_n > 20$ MeV). However, when considering the ILL-H7 site, and its averaged artificial overburden of 15 m.w.e. (see Sect. 5.2), we see that most thermal and cascade neutrons are cut-out and that the evaporation neutron population has shifted to lower energies with its peak at around 1 MeV. Though significantly reduced with respect to an unshielded surface lab, we still observe some high energy neutrons up to 200 MeV that can still affect the future RICOCHET experiment sensitivity. Regarding the reactogenic IN20 model (red histogram), we see that its MeV-scale neutron flux is more than one order of magnitude larger than its cosmogenic counterpart (green histogram), but it also exhibits a much lower energy end point of 6 MeV suggesting that it should be better attenuated by the RICOCHET shielding.

5 Fast neutron flux characterizations

This section is the core of our work as it discusses how our simulated neutron backgrounds compare with our experi-

mental observations with the ^3He proportional counter presented in Sect. 3. It is worth emphasizing that no parameter of the reactogenic and cosmogenic neutron flux models was tuned to better reproduce the observed spectra. Therefore, both neutron flux models have been used as is to compute our expected RICOCHET neutron background presented in Sect. 6.

5.1 Validation of the method: the IP2I fast neutron background

As a proof of concept of our proposed neutron background assessment methodology we first studied the case of the IP2I surface lab. The latter is located in Lyon at an altitude of 181 m above sea level and at a latitude of $45^\circ 45' 32.616''$ North. The modelization of the cryogenic lab in our CRY simulations considers that it is in the basement of a two-story high building made of thick concrete walls and floors. We found that the main overburden comes from the floor and ceiling above our experimental area, which amounts to 1.2 m of concrete and consequently provides about 2.76 m.w.e. of direct vertical overburden. Additionally, the near proximity of our detectors to a 1.45 m-thick concrete wall provides an additional position dependent solid angle-integrated overburden.

In order to properly compare our cosmogenic simulations to our observations with both the ^3He proportional counter and the Ge bolometers operated in the same lab, about 3 m away from each other, we first estimated the common overburden with the use of muon flux attenuation measurements. To do so, we used 1 cm thick, 20 cm long, and 5 cm wide plastic scintillator panels arranged in a 4×4 array from the muography research team in IP2I [31]. The energy loss from the muons going through the panels is converted into scintillation photons which are guided towards a multi-anode photomultiplier by wavelength-shifting optical fibres. Muons were identified as such by requiring coincident triggers on all four plastic scintillators planes. In order to confirm the IP2I building geometry utilized in the simulations for the neutron background assessment, we measured the muon rates at three different locations and derived an averaged overburden. The first position was next to the ^3He counter but closer to the thick wall (maximizing the effective overburden). The second position was 3 m away against the opposing thin wall next to the windows (minimizing the effective overburden). Lastly, the third position was above the cryostat where the Ge detectors were operated. Therefore, the latter position is the most relevant while the first two ones can be considered as being the upper and lower bounds on the surface lab overburden.

Figure 6 shows the time evolution of the observed muon trigger rates at these three locations within our cryogenic lab (purple, orange, and brown dots) and from the roof of the building (green dots) to determine a zero-overburden reference measurement. Also shown is the time dependent atmo-

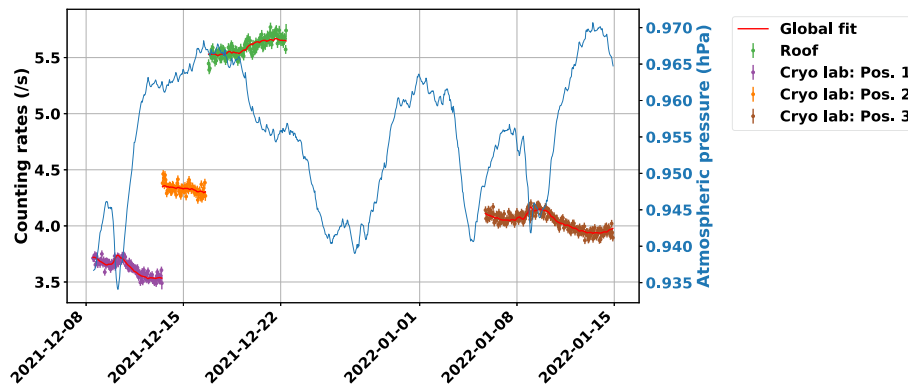


Fig. 6 Time evolution of the muon trigger rate at three different locations in our IP2I cryogenic lab (purple, orange, and brown dots) and from the roof of the building to determine the muon trigger rate with no overburden (green dots). The blue curve shows the evolution in time of

the atmospheric pressure as extracted from the ERA5 global reanalysis hourly data [30]. The latter was taken into account in our determination of the mean muon trigger rates at each locations within our fitting procedure (red line)

spheric pressure (blue line) which was used in our fitting model (red line) to derive a mean muon trigger rate at each location. Thanks to the muon trigger rate from the roof, we can derive the muon flux attenuations a_μ at the three cryogenic lab locations which were found to be of: 0.63 ± 0.01 (position 1), 0.78 ± 0.01 (position 2), and 0.72 ± 0.01 (position 3). Following the procedure described in [33], corresponding overburdens m_0 can be estimated from the observed muon flux attenuation factors a_μ using the approximation below from [34]:

$$a_\mu = 10^{-1.32 \log d - 0.26 (\log d)^2} \quad (2)$$

where $d = 1 + m_0/10$, and m_0 is given in meter water equivalent (m.w.e.). The derived overburden values at each of these locations were thus found to be: 4.05 ± 0.16 m.w.e. (position 1), 2.04 ± 0.11 m.w.e. (position 2), and 2.76 ± 0.13 m.w.e. (position 3), leading to an averaged overburden in our lab considered hereafter of 2.95 ± 0.65 m.w.e. Interestingly, attenuations obtained from our CRY simulations of the muon panel setups at position 1 and 2 of the I2PI lab were found to be 0.65 and 0.78, respectively, which supports the IP2I geometry used hereafter.

Figure 7 (left panel) shows the comparison between the observed and simulated ^3He spectra obtained at the IP2I surface lab. The measured energy spectrum (red histogram) has been obtained by subtracting the observed event rate from LSM in order to remove the internal background of the detector (see Sect. 3). As one can conclude from Fig. 7 (left panel), the observed and simulated spectra match almost perfectly well over the entire energy range relevant for fast neutron flux measurements (i.e. for detected energies above 1 MeV). We indeed found integrated rates between 1 and 4.5 MeV of 24.5 ± 0.9 and 23.7 ± 1.4 per day from the simulated and observed energy spectra, respectively. This suggests that both

the magnitude and energy dependence of the fast neutron flux entering the ^3He proportional counter is well estimated by our simulations up to about 4.5 MeV in detected energy – limited by the ^3He proportional counter’s internal background subtraction limit shown as the gray contour. The latter represents the 95% C.L. limit on the significance of the neutron detection rate, calculated using the impact of Poisson fluctuations on the internal background subtraction described in Sect. 3.

In order to further validate this cosmogenic neutron flux model, we propagated it to 38 g Ge cryogenic bolometers operated in a dry dilution cryostat surrounded by a 70%-coverage 10 cm thick cylindrical lead shielding with a 7 cm thick bottom end-cap. Figure 7 (right panel) shows the comparison between the observed recoil energy spectra from our prototype bolometers called RED20 [32] (black solid line) and from RED80, which has the ability to discriminate electronic recoils (red) from nuclear ones (blue) [14], and the simulated cosmogenic background (filled histograms). Note that our simulations do not take into account internal and external radioactivity from the surrounding materials which are likely to also contribute to the total background, especially with an incomplete lead shielding as considered here. Also, the cryogenic Ge bolometers were calibrated using a ^{55}Fe source emitting 5.89 and 6.49 keV X-rays for RED20, and internal ^{71}Ge electron-capture decays emitting low-energy X-rays of 10.37 and 1.3 keV following a thermal neutron activation of the RED80 detector. Overall, from 1 to 15 keV we see that the total observed and simulated recoil spectra agree within a factor of about three.² Thanks to RED80, which

² The steep rise in the energy spectrum below 1 keV, so-called low-energy excess, is the subject of ongoing intense worldwide investigations. For more details, see [35] Additionally, note that the sharp rise at 1.5 keV in RED80 is due to the 1.3 keV X-ray line from ^{71}Ge electron-capture decays.

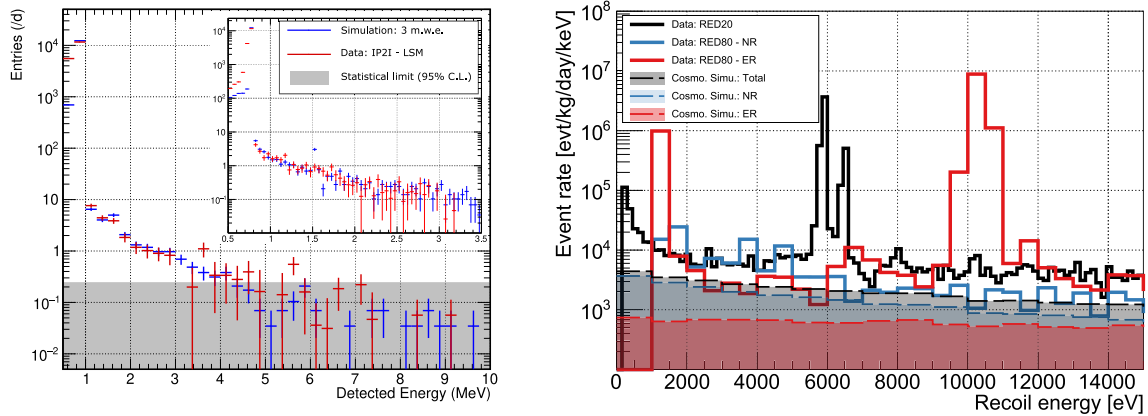


Fig. 7 Left: comparison of the simulated (blue) and the observed (red) ^3He proportional counter data while operated at the IP2I surface lab after 18 days of data taking. The red histogram has been obtained by subtracting the observed spectra from the LSM to subtract the internal alpha background of the detector. The simulation considers the IP2I building geometry discussed in the text with its averaged overburden of 3 m.w.e. as estimated from our muon flux attenuation measurements. As discussed in Sect. 3, due to the internal proportional counter background, a statistically significant neutron contribution can be inferred from an observed rate larger than about 0.25 evt/day/bin at 95% C.L. Right: comparison between the observed data with the RED20 [32] and

RED80 [14] low-threshold cryogenic detectors, operated in the IP2I cryostat surrounded by a 70% coverage 10 cm thick lead shielding, and its resulting cosmogenic background simulation. For both the simulation and the RED80 data, we show the nuclear (blue) and electronic (red) recoil components, as well as the total expected cosmogenic background at IP2I (black dashed curve). Note that the remaining internal and external radioactivity from the surrounding materials are not taken into account here. For the sake of clarity, error bars are not shown but are about 10% [32] and 30% [14] for the RED20 and RED80 data, respectively

benefits from particle identification capability with its double heat-and-ionization readout, we see that this disagreement is about a factor of six for the gammas and three for the neutrons. However, it is worth noticing that the simulation reproduces well the different slopes of the observed electronic and nuclear recoil spectra. The gamma discrepancy is most likely explained by an underestimation of the gamma background in our cosmogenic-only simulations where radiogenic contributions are not taken into account while they are likely to be significant. Indeed, removing the lead shielding around the cryostat increases the electronic recoil rate in the bolometers by a factor ten, while a more optimized shielding should provide order of magnitude better protection from gamma rays [36]. The observed excess of the electronic recoil rate compared to a simulation restricted to cosmogenic gammas is thus not surprising. The factor of three discrepancy between the simulations and the observations regarding the neutron component is however still under investigation. For instance, some plausible explanations could be that our IP2I experimental setup simulation is oversimplified, or that our cryogenic lab exhibits a larger than expected epithermal neutron population escaping our ^3He proportional counter sensitivity operated 3 m away from the IP2I cryostat. Indeed, it is worth noting that in such a configuration the bare ^3He is probing almost exclusively the neutron evaporation peak (see Fig. 5), while the bolometers are also sensitive to the cascade peak

as the neutrons get down-converted to lower energies thanks to the lead shielding surrounding the cryostat. Such neutrons would then induce a larger than expected keV-scale nuclear recoil rate in our bolometers. We plan to test this hypothesis using lithiated bolometers [37,38], operated in our cryostat at IP2I, and hydrogen recoil proportional counters which should exhibit complementary epithermal neutron sensitivity to our ^3He detector. Also, following the approach from [39], the RICOCHET Collaboration is investigating the possibility to use Bonner spheres to characterize the cosmogenic neutron flux up to the 100 MeV-scale at both the IP2I and ILL sites to further assess the high energy end of the cosmogenic neutron fluxes.

Eventually, the qualitative concordance between the simulated and observed nuclear recoil background with the Ge bolometers confirms the reliability of our proposed neutron background assessment approach using a ^3He proportional counter combined with both muon flux attenuation measurements and CRY-based simulations. Quantitatively it appears that in the case of our cryogenic lab at IP2I, with a measured ~ 3 m.w.e. overburden and no polyethylene shielding around the cryostat, we are underestimating the neutron background at the Ge bolometers by a factor of about three. Provided that such a scaling factor is conserved between the two setups at IP2I and ILL, we will consider it as the worst case scenario of our Ricochet sensitivity study presented in Sect. 6.

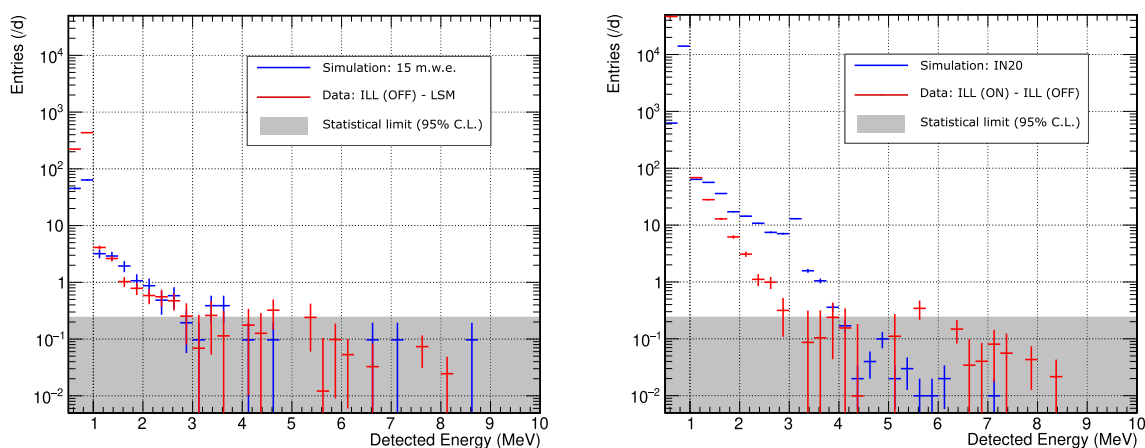


Fig. 8 Left: comparison between the observed ^3He energy spectra of the cosmogenic neutron background at the ILL-H7 site after 40.7 days of data taking (red) and its corresponding simulations (blue). Note that the red histogram has been obtained by subtracting the LSM data in order to remove the internal alpha background contamination. Right: comparison between the observed ^3He energy spectra of the reactogenic neutron background at the ILL-H7 site after 46.3 days of data taking with an averaged reactor power of 42 MW (red) and its corresponding simulations (blue). Note that the red histogram has been obtained

by subtracting the reactor OFF data, which subtracts both the residual internal background contamination and the cosmogenic component within statistical uncertainties. All measurements at the ILL reactor were done with a 1 cm thick layer of boron-loaded rubber around the ^3He proportional counter. Lastly, as discussed in Sect. 3, due to the internal proportional counter background, a statistically significant neutron contribution can be inferred from an observed rate larger than about 0.25 evt/day/bin at 95% C.L.

5.2 RICOCHET fast neutron background characterization: cosmogenic and reactogenic neutrons at the ILL-H7 site

At the end of 2020, the STEREO experiment was decommissioned. Since then, the ILL-H7 site has been empty and therefore perfectly well-suited for background and on-site characterizations prior to the RICOCHET integration. Starting in January 2021, we took almost a hundred days worth of data, during reactor ON and OFF periods, with the ^3He proportional counter located at the planned position of the RICOCHET cryostat. To properly simulate the ILL site, we used the altitude and latitude of Grenoble which are 212 m above sea level and $45^\circ 11' 18.704''$ North, respectively, and also applied the 1.28 cosmic flux normalization factor from STEREO (see Sect. 4.2).

Figure 8 (left panel) shows the resulting comparison between the cosmogenic simulations (blue) and the observed data (red) of the ^3He detector at the ILL-H7 site when the reactor is OFF. Similarly to the IP2I case, the red histogram has been obtained after subtraction of the event rate observed from the LSM data in order to subtract the residual internal background. Again, an excellent agreement between the experimental data and the cosmogenic simulations is observed above 1 MeV in detected energy. We indeed found integrated rates between 1 and 4.5 MeV of 12.2 ± 1.1 and 11.1 ± 0.8 per day from the simulated and observed energy spectra respectively, hence validating our cosmogenic neutron flux model to be used to estimate the corresponding neutron background to the future RICOCHET experiment.

Data with our proportional counter was also acquired during reactor ON periods in order to estimate the reactogenic neutron flux. Figure 8 (right panel) presents the resulting reactogenic neutron data and simulations. The experimental data (red histogram) has been derived by subtracting the OFF period to remove both the cosmogenic neutrons and the residual internal background contributions. The simulated spectrum (blue) has been obtained by scaling the spectrum from IN20 in Fig. 5 (red histogram) to the reduced 42 MW thermal power during our measurements. First, it is worth noticing that we observe a fast neutron detection rate about 10 times higher during reactor ON periods (121.9 ± 1.9 per day) with respect to OFF periods (11.5 ± 0.9 per day), for that reactor power of 42 MW and IN20 in operation. Taken at face value, this suggests an overall reactogenic fast neutron flux about 15 times higher than the cosmogenic one when the reactor is operated at its full 58 MW nominal thermal power. Note that a higher reactogenic fast neutron flux is also expected from Fig. 5. Also, in this case we observe a significant departure between the two histograms, suggesting that our simulated reactogenic neutron flux is both too high and at higher energies than what we observe. Similarly, our simulations predict a fast neutron detection rate of about 230 per day above 1 MeV, hence almost two times higher than the observed one. This difference can be explained by the fact that the IN20 neutron spectrum considered here doesn't take into account the lead and polyethylene walls that are surrounding the ILL-H7 site, nor the neutron moderator and shielding from the IN20 instrument. As suggested in Sect. 4.2, it was indeed expected

that our neutron background model assumption, using the outgoing IN20 reactogenic neutron flux from the H13 beam, would overestimate the fast neutron flux at the RICOCHET location. However, in order to provide some conservative estimates of the expected neutron background, we consider hereafter this un-moderated IN20 neutron flux as an input to our RICOCHET background simulations.

6 RICOCHET expected neutron background

From the cosmogenic and reactogenic neutron components of the expected RICOCHET background – compared against the ³He counter data in the previous section (see Sect. 5) – we can estimate the expected RICOCHET neutron background using a GEANT4 simulation taking into account its entire shielding and detector geometry, introduced in Sect. 2.

Table 1 presents the resulting expected reactogenic and cosmogenic neutron background rates, integrated over our CENNS region of interest between 50 eV and 1 keV, for various shielding configurations: (I) no shielding, (II) with the passive shielding presented in Fig. 1, and (III) with the addition of an idealized muon veto assumed to have a 100% geometrical and detection efficiency surrounding the RICOCHET experimental setup. Additionally, we also show in Fig. 9 the resulting energy spectra for both the CENNS signal (green) and the two nuclear recoil background components, i.e. cos-

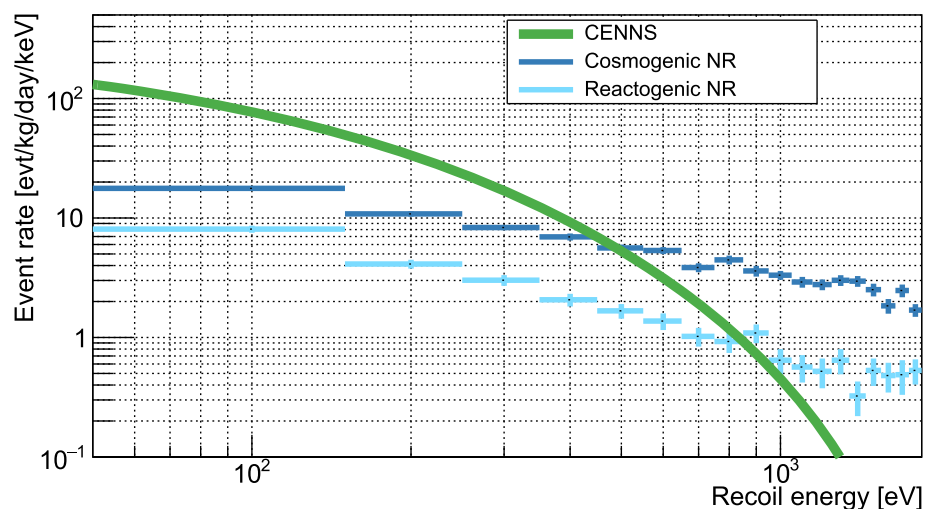
mogenic (dark blue) and reactogenic (light blue), considering the shielding configuration (III). From the comparison of the first two shielding configurations I and II presented in Table 1, one can derive that the neutron background attenuation factors provided by the passive RICOCHET shielding are about 37 and of the order of 10⁴ for the cosmogenic and reactogenic neutron backgrounds, respectively. The much greater attenuation factor for reactogenic neutrons is explained by both (1) the absence of muon-induced spallation in the shielding producing fast neutrons in close proximity to the detectors, and (2) their comparatively low energy when compared to that of primary and spallation neutrons from the cosmogenic contribution as they enter the RICOCHET shielding. Indeed, most of these reactogenic neutrons have kinetic energies below 6 MeV (see Fig. 5), corresponding to a mean free path in polyethylene of about 6 cm, making them efficiently moderated by the 35 cm of polyethylene. On the other hand, with energies up to ~ 200 MeV as obtained after spallation in the ILL building, cosmogenic neutrons in the casemate can still spallate further and reach the RICOCHET cryogenic detectors. Interestingly, by tracking backwards to the primary cosmic rays above ILL, we found that all primary cosmic neutrons inducing nuclear recoils in our Ge bolometer had energies greater than 70 MeV and represented about 13% of the total number of cosmogenic nuclear recoils, the rest being largely dominated by muon spallations (85%). Therefore, despite their higher expected (and measured) overall fast neutron

Table 1 Simulated background rates inside the cryogenic detector array installed at the ILL, with the shielding design illustrated in Fig. 1, when only one bolometer has triggered. As the muon veto is still being char-

acterized and optimized, in the case of scenario (III) we assume perfect geometrical and detection efficiencies

	Cosmogenic	Reactogenic	Total (MC)	CENNS (Ge/Zn)
Nuclear recoils [50 eV, 1 keV] (evts/day/kg)				
No shielding (I)	1554 ± 12	53853 ± 544	55407 ± 545	–
Passive shielding (II)	42 ± 3	2.4 ± 0.3	44 ± 3	–
Passive + μ-veto (III)	7 ± 2		9 ± 2	12.8 / 11.2

Fig. 9 Simulated energy spectra for the future RICOCHET experiment at ILL, 8.8 m away from the core of the 58.3 MWth nuclear reactor. The CENNS signal is given by the green distribution while the resulting nuclear recoil background from the cosmogenic and reactogenic components correspond respectively to the dark and light blue histograms. The presented background simulation results correspond to the shielding configuration (III), see Table 1



flux, reactogenic neutrons are not expected to be a dominant background to the future RICOCHET experiment even when considering the extreme case of the un-moderated IN20 simulated neutron flux (see Sect. 5.2). However, note that reaching such high attenuation factors puts strong constraints on the tightness of the passive shielding, hence the additional internal layers between the thermal screens to limit possible neutron leakage to the bolometers from the top (see Sect. 2).

The comparison of the shielding configurations II and III from Table 1 suggests that an idealized muon veto could help reducing the cosmogenic neutron background by an additional factor of 6. As the RICOCHET muon veto won't be as efficient as an ideal one, we indeed expect an overall muon veto tagging efficiency of about 90%, we consider hereafter that our cosmogenic neutron background will be between 42 ± 3 and 7 ± 2 events per day. Solely considering the expected neutron backgrounds, these two cases respectively lead to signal-to-background ratios of about 0.3 and 1.4. Assuming a 70% CENNS detection efficiency, arising from estimated livetime loss and of various analysis cuts finite efficiencies, these values suggest that the RICOCHET experiment could reach a statistical CENNS detection significance³ after only one reactor cycle between 7.5σ and 13.6σ . If we apply a conservative factor of 3 to the neutron background rates based on the Ge bolometer comparison between our cosmogenic simulations and observations done at IP2I (see Sect. 5.1), these significances drop to 4.6σ and 9.2σ depending on the muon veto efficiency, respectively. It is worth mentioning that more sophisticated data analysis methods, considering the difference in the shape of the CENNS and background energy spectra (see Fig. 9), should lead to greater statistical significance. This is part of an ongoing study, also taking into account the finite resolution of the detector and related analysis cuts, that will be presented in a forthcoming paper.

Lastly, it is worth highlighting that these neutron background based sensitivity estimates assume that there are no additional unexpected backgrounds, and that the gamma background will be both low enough and efficiently rejected thanks to the RICOCHET bolometers' particle identification capabilities.

7 Conclusion

In this paper, we have presented our fast neutron flux characterization with a dedicated low-background ³He proportional counter. We first tested our method by comparing simulated and observed energy spectra from the IP2I sur-

face lab where cryogenic detectors, with particle identification capabilities, were also operated. This allowed us to cross-check that our cosmogenic simulations were properly reproducing both the ³He spectra above 1 MeV in detected energy and the low-energy nuclear recoil spectrum from our Ge bolometers to within a factor of about three, assuming a sole cosmogenic neutron component. Following this cross-validation, we measured and simulated the neutron fluxes at the ILL-H7 site, where the future CENNS RICOCHET experiment will be deployed. Firstly, we found an excellent agreement between our cosmogenic neutron simulation and measurements. Based on these observations, one can conclude that CRY provides reliable estimates of cosmogenic backgrounds for experiments located at shallow sites with depths from 3 to 15 m.w.e. Secondly, a significant disagreement has been found in the case of reactogenic neutrons between our ³He simulations and experimental data, suggesting that the IN20 neutron model considered here overestimates the reactor induced neutron energies and flux at the ILL-H7 site. Therefore, the IN20 neutron flux model is considered as a conservative model to estimate the anticipated reactogenic neutron background for RICOCHET. Following these onsite neutron background characterizations, we propagated both our reactogenic and cosmogenic neutron fluxes into our RICOCHET shielding simulation to estimate its expected nuclear recoil background level. Interestingly, despite its higher fast neutron flux, we found that the reactogenic neutron background will only contribute to about one fourth of the overall RICOCHET neutron background, suggesting that the ON/OFF reactor modulations should lead to an increased CENNS sensitivity. Considering only our neutron background model, compared against experimental data from an ensemble of detectors and sites, we found that the statistical significance of a CENNS detection with RICOCHET, after only one reactor cycle, should be between 4.6 and 13.6σ , depending on the effectiveness of the muon veto. A similar study dedicated to the gamma induced background, also addressing the particle identification capabilities of our detectors, is ongoing and will be presented in a forthcoming paper. Furthermore, we plan to measure the background level inside the final RICOCHET shielding before the installation of the cryostat end of 2023.

Acknowledgements We are grateful to the EDELWEISS Collaboration for the use of its electronics and DAQ system in the operation of the RED20 and RED80 cryogenic detectors discussed in Sect. 5. We are also thankful to Jacques Marreau for his help in operating and analysing the data from the muon panels of his muography research team in IP2I. This project has received funding from the European Research Council (ERC) under the European Union's Horizon 2020 research and innovation program under Grant Agreement ERC-StG-CENNS 803079, the French National Research Agency (ANR) within the project ANR-20-CE31-0006, the LabEx Lyon Institute of Origins (ANR-10-LABX-0066) of the Université de Lyon, the NSF under Grant PHY-2013203. A portion of the work carried out at MIT was supported

³ The significance is defined as $Z = S/\sqrt{(S+2B)}$ with S and B the numbers of CENNS and background events respectively and assuming equal reactor ON and OFF exposition times.

by DOE QuantISED award DE-SC0020181 and the Heising-Simons Foundation. This work is also partly supported by the Ministry of science and higher education of the Russian Federation (the contract no. 075-15-2020-778).

Data Availability Statement This manuscript has associated data in a data repository. [Authors' comment: All data included in this manuscript are available upon request by contacting the corresponding author.]

Open Access This article is licensed under a Creative Commons Attribution 4.0 International License, which permits use, sharing, adaptation, distribution and reproduction in any medium or format, as long as you give appropriate credit to the original author(s) and the source, provide a link to the Creative Commons licence, and indicate if changes were made. The images or other third party material in this article are included in the article's Creative Commons licence, unless indicated otherwise in a credit line to the material. If material is not included in the article's Creative Commons licence and your intended use is not permitted by statutory regulation or exceeds the permitted use, you will need to obtain permission directly from the copyright holder. To view a copy of this licence, visit <http://creativecommons.org/licenses/by/4.0/>.

Funded by SCOAP³. SCOAP³ supports the goals of the International Year of Basic Sciences for Sustainable Development.

References

1. D.Z. Freedman, Phys. Rev. D **9**, 1389 (1974). <https://doi.org/10.1103/PhysRevD.9.1389>
2. D. Akimov et al., Science **357**(6356), 1123 (2017). <https://doi.org/10.1126/science.aao0990>
3. J. Billard, J. Johnston, B.J. Kavanagh, JCAP **11**, 016 (2018). <https://doi.org/10.1088/1475-7516/2018/11/016>
4. A. Aguilar-Arevalo et al., J. Phys. Conf. Ser. **761**(1), 012057 (2016). <https://doi.org/10.1088/1742-6596/761/1/012057>
5. S. Kerman, V. Sharma, M. Deniz, H. Wong, J.W. Chen, H. Li, S. Lin, C.P. Liu, Q. Yue, Phys. Rev. D **93**(11), 113006 (2016). <https://doi.org/10.1103/PhysRevD.93.113006>
6. V. Belov et al., JINST **10**(12), P12011 (2015). <https://doi.org/10.1088/1748-0221/10/12/P12011>
7. H. Bonet, et al., Constraints on elastic neutrino nucleus scattering in the fully coherent regime from the CONUS experiment. Phys. Rev. Lett. **126**(4), 041804 (2021). <https://doi.org/10.1103/PhysRevLett.126.041804>
8. J. Colaresi, J.I. Collar, T.W. Hossbach, C.M. Lewis, K.M. Yocum, Phys. Rev. Lett. **129**, 211802 (2022). <https://doi.org/10.1103/PhysRevLett.129.211802>
9. G. Agnolet et al., Nucl. Instrum. Methods A **853**, 53 (2017). <https://doi.org/10.1016/j.nima.2017.02.024>
10. R. Strauss et al., Eur. Phys. J. C **77**, 506 (2017). <https://doi.org/10.1140/epjc/s10052-017-5068-2>
11. C. Augier, et al., in *19th International Workshop on Low Temperature Detectors* (2021)
12. D. Akimov et al., First measurement of coherent elastic neutrino-nucleus scattering on argon. Phys. Rev. Lett. **126**(1), 012002 (2021). <https://doi.org/10.1103/PhysRevLett.126.012002>
13. D. Baxter et al., JHEP **02**, 123 (2020). [https://doi.org/10.1007/JHEP02\(2020\)123](https://doi.org/10.1007/JHEP02(2020)123)
14. D. Misiak, Développements de nouveaux détecteurs cryogéniques bas seuils pour la recherche de matière noire légère et la physique des neutrinos de basse énergie. Theses, Université de Lyon (2021). <https://tel.archives-ouvertes.fr/tel-03328713>
15. J. Billard, Searching for dark matter and new physics in the neutrino sector with cryogenic detectors. Habilitation à diriger des recherches, Université Claude Bernard Lyon 1 (2021). <https://tel.archives-ouvertes.fr/tel-03259707>
16. N. Allemandou et al., JINST **13**(07), P07009 (2018). <https://doi.org/10.1088/1748-0221/13/07/P07009>
17. H. Almazán, et al., Interpreting reactor antineutrino anomalies with STEREO data (2022). [arXiv: 2210.07664](https://arxiv.org/abs/2210.07664)
18. D. Brown, M. Chadwick, R. Capote, A. Kahler, A. Trkov, M. Herman, A. Sonzogni, Y. Danon, A. Carlson, M. Dunn, D. Smith, G. Hale, G. Arbanas, R. Arcilla, C. Bates, B. Beck, B. Becker, F. Brown, R. Casperson, J. Conlin, D. Cullen, M.A. Descalle, R. Firestone, T. Gaines, K. Guber, A. Hawari, J. Holmes, T. Johnson, T. Kawano, B. Kiedrowski, A. Koning, S. Kopecky, L. Leal, J. Lestone, C. Lubitz, J. Márquez Damián, C. Mattoon, E. McCutchan, S. Mughabghab, P. Navrátil, D. Neudecker, G. Nobre, G. Noguere, M. Paris, M. Pigni, A. Plompen, B. Pritychenko, V. Pronyaev, D. Roubtsov, D. Rochman, P. Romano, P. Schillebeeckx, S. Simakov, M. Sin, I. Sirakov, B. Sleaford, V. Sobes, E. Soukhovitskii, I. Stetcu, P. Talou, I. Thompson, S. van der Marck, L. Welsch-Sherrill, D. Wiarda, M. White, J. Wormald, R. Wright, M. Zerkle, G. Žerovnik, Y. Zhu, Nucl. Data Sheets **148**, 1 (2018). <https://doi.org/10.1016/j.nds.2018.02.001>. (special issue on nuclear reaction data)
19. A.R. Sayres, K.W. Jones, C.S. Wu, Phys. Rev. **122**, 1853 (1961). <https://doi.org/10.1103/PhysRev.122.1853>
20. G. Vidyakin et al., Prib. Tekh. Eksp. **32**, 70 (1989)
21. F. Ziegler, M. Ziegler, J. Biersack, Nucl. Instrum. Methods **B268**, 1818–1823 (2010)
22. R. Lemrani, M. Robinson, V.A. Kudryavtsev, M. De Jesus, G. Gerbier, N.J.C. Spooner, Nucl. Instrum. Methods A **560**, 454 (2006). <https://doi.org/10.1016/j.nima.2005.12.238>
23. S. Rozov, et al., Monitoring of the thermal neutron flux in the LSM underground laboratory (2010). [arXiv: 1001.4383](https://arxiv.org/abs/1001.4383)
24. A. Leder et al., JINST **13**(02), P02004 (2018). <https://doi.org/10.1088/1748-0221/13/02/P02004>
25. J. Allison et al., Nucl. Instrum. Methods A **835**, 186 (2016). <https://doi.org/10.1016/j.nima.2016.06.125>
26. M.H. Mendenhall, R.A. Weller, Nucl. Instrum. Methods Phys. Res. Sect. B **227**(3), 420–430 (2005). <https://doi.org/10.1016/j.nimb.2004.08.014>
27. C. Hagmann, D. Lange, D. Wright, in *2007 IEEE Nuclear Science Symposium Conference Record*, vol. 2 (2007), pp. 1143–1146. <https://doi.org/10.1109/NSSMIC.2007.4437209>
28. M. Pequignot, Les expériences Nucifer et Stéréo : étude des antineutrinos de réacteurs à courte distance. Theses, Université Paris Sud - Paris XI (2015). <https://tel.archives-ouvertes.fr/tel-01217946>
29. L.S. Waters, G.W. McKinney, J.W. Durkee, M.L. Fensin, J.S. Hendricks, M.R. James, R.C. Johns, D.B. Pelowitz, AIP Conf. Proc. **896**(1) (2007). <https://doi.org/10.1063/1.2720459>. <https://www.osti.gov/biblio/21055006>
30. H. Hersbach, et al., Era5 hourly data on single levels from 1979 to present. <https://cds.climate.copernicus.eu/cdsapp#!/dataset/reanalysis-era5-single-levels?tab=overview>. Accessed 15 Jan 2022
31. J. Marteau, J.D.B. d'Ars, D. Gibert, K. Jourde, J.C. Ianigro, B. Carlus, JINST **12**(02), C02008 (2017). <https://doi.org/10.1088/1748-0221/12/02/C02008>
32. E. Armengaud et al., Phys. Rev. D **99**(8), 082003 (2019). <https://doi.org/10.1103/PhysRevD.99.082003>
33. G. Angloher et al., Eur. Phys. J. C **79**(12), 1018 (2019). <https://doi.org/10.1140/epjc/s10052-019-7454-4>
34. P. Theodorsson, *Measurement of Weak Radioactivity* (World Scientific, Singapore, 1996)
35. A. Fuss, M. Kaznacheeva, F. Reindl, F. Wagner (Eds.), *EXCESS Workshop: Descriptions of Rising Low-energy Spectra* (2022)

36. G. Heusser, M. Weber, J. Hakenmüller, M. Laubenstein, M. Lindner, W. Maneschg, H. Simgen, D. Stolzenburg, H. Strecker, *Eur. Phys. J. C* **75**(11), 531 (2015). <https://doi.org/10.1140/epjc/s10052-015-3704-2>
37. N. Coron et al., *J. Phys. Conf. Ser.* **375**, 012018 (2012). <https://doi.org/10.1088/1742-6596/375/1/012018>
38. E. Armengaud et al., *Eur. Phys. J. C* **77**(11), 785 (2017). <https://doi.org/10.1140/epjc/s10052-017-5343-2>
39. J. Hakenmüller et al., *Eur. Phys. J. C* **79**(8), 699 (2019). <https://doi.org/10.1140/epjc/s10052-019-7160-2>